Numerical and experimental study of dissociation in an air-water single-bubble sonoluminescence system

Gabriela F. Puente, Raúl Urteaga, and Fabián J. Bonetto
Laboratorio de Cavitación y Biotecnología Instituto Balseiro/Centro Atómico Bariloche, 8400 San Carlos de Bariloche, Rio Negro, Argentina
(Received 8 October 2004; published 10 October 2005)

We performed a comprehensive numerical and experimental analysis of dissociation effects in an air bubble in water acoustically levitated in a spherical resonator. Our numerical approach is based on suitable models for the different effects considered. We compared model predictions with experimental results obtained in our laboratory in the whole phase parameter space, for acoustic pressures from the bubble dissolution limit up to bubble extinction. The effects were taken into account simultaneously to consider the transition from nonsonoluminescence to sonoluminescence bubbles. The model includes (1) inside the bubble, transient and spatially nonuniform heat transfer using a collocation points method, dissociation of O_2 and N_2, and mass diffusion of vapor in the noncondensable gases; (2) at the bubble interface, nonequilibrium evaporation and condensation of water and a temperature jump due to the accommodation coefficient; (3) in the liquid, transient and spatially nonuniform heat transfer using a collocation points method, and mass diffusion of the gas in the liquid. The model is completed with a Rayleigh-Plesset equation with liquid compressible terms and vapor mass transfer. We computed the boundary for the shape instability based on the temporal evolution of the computed radius. The model is valid for an arbitrary number of dissociable gases dissolved in the liquid. We also obtained absolute measurements for $R(t)$ using two photodetectors and Mie scattering calculations. The robust technique used allows the estimation of experimental results of absolute R_0 and P_a. The technique is based on identifying the bubble dissolution limit coincident with the parametric instability in (P_a,R_0) parameter space. We take advantage of the fact that this point can be determined experimentally with high precision and replicability. We computed the equilibrium concentration of the different gaseous species and water vapor during collapse as a function of P_a and R_0. The model obtains from first principles the result that in sonoluminescence the bubble is practically 100% argon for air dissolved in water. Therefore, the dissociation reactions in air bubbles must be taken into account for quantitative computations of maximum temperatures. The agreement found between the numerical and experimental data is very good in the whole parameter space explored. We do not fit any parameter in the model. We believe that we capture all the relevant physics with the model.

DOI: 10.1103/PhysRevE.72.046305 PACS number(s): 78.60.Mq

I. INTRODUCTION

The numerical models associated with single-bubble sonoluminescence (SBSL) can be classified in two categories: Models that take into account the spatial and temporal dependence of the different variables with hundreds of spatial nodes using partial differential equations (PDE's) and models that require the solution of a system of ordinary differential equations [1]. Among the first category we can cite Wu and Roberts [2], Moss *et al.* [3], Storey and Szeri [4], and Storey [5]. These models produce the best results but they are typically solved for one acoustic cycle. They are also computationally expensive and it is not realistic to perform parametric runs for the number of cycles in each run needed for this work. In this paper we used the Keller version of the Rayleigh-Plesset equation (RPE) [6–9] generalized for mass transfer at the bubble interface.

Hao and Prosperetti [10] performed transient and spatially nonuniform heat transfer calculations inside the bubble using a collocation points method. We used this technique for low acoustic pressures ($P_a \approx 1.2$ bar). For acoustic pressures higher than approximately 1.2 bar the thermal boundary layer is small enough that the approximation used by Toegel *et al.* [11] is very good. In fact we compared the results of these two approaches for a pressure. $P_a = 1.2$ bar and the results are very similar [1% mean error in $R(t)$].

Kamath *et al.* [12] performed calculations using a transient chemical reaction model for the vapor that was compatible with the use of a RPE. The same model was used by Yasui [9]. Toegel and Lohse [13] used a model along these lines for the computation of dissociation effects in noncondensable gases. We used a similar model to take into account the N_2 and O_2 dissociation.

Yasui [9] also presented a model valid when nonequilibrium evaporation and condensation is present at the interface. The model accounts for the temperature discontinuity and the net vapor mass transfer using the accommodation coefficient. We used this scheme in our model. Toegel and Lohse [13] did not take this effect into account.

Hao and Prosperetti [10] used the collocation method to solve the energy equation in the liquid [14]. Toegel *et al.* [15], on the other hand, assumed that the liquid temperature at the interface was equal to the liquid temperature far from the bubble based on analysis performed by Kamath *et al.* [16]. Hilgenfeldt *et al.* [17] solved the gas mass conservation equation in the liquid coupled to the RPE solution, obtaining

the diffusive stability points in the (R_0, P_a) phase plane.

The bubble phase space has also been experimentally studied [18]. Different techniques have been used to estimate the temporal evolution of the absolute value of the bubble radius and the acoustic pressure but the most common are based on a RPE fit [19] of the light scattered by a laser illuminated bubble.

Ketterling and Apfel [20] performed an extensive mapping of the phase space for non-SL and SL bubbles for several gases in water. They used a stroboscopic imaging system to measure the temporal evolution of the bubble radius. They determine the ambient radius as the bubble radius that corresponded to a zero value (negative slope) for the acoustic pressure. The acoustic pressure was established from a RPE fit to the measured maximum radius and the estimated ambient radius. In these measurements the estimated error in R_0 was ± 1 μm and the error in P_a was ± 0.025 bar.

Eller and Crum [21] computed the shape instability threshold. Hilgenfeldt *et al.* [17] obtained the shape instability for bubbles with imposed concentrations instead of considering the ambient radius known. Hao and Prosperetti [10] computed shape instability thresholds taking into account the effects of viscosity and vorticity. We followed Hao and Prosperetti in our calculations without taking the effect of the vorticity into account. See [10] for a discussion of the effect of the vorticity on the bubble shape instability.

In this work we present a complete model for the temporal evolution of the bubble radius for SBSL bubbles and non-SL bubbles. The model is valid for an arbitrary number of dissociable gases dissolved in the liquid. We also present experimental results of bubble radius temporal evolutions, ambient radius, and acoustic pressures with unprecedented small uncertainties due to the accuracy, precision, and replicability in the determination of the values of R_0 and P_a at the dissolution point. We also present a detailed comparison between experimental and numerical results.

II. EXPERIMENT

For the experimental measurements we used a typical setup of sonoluminescence. Figure 1 shows a schematic of our setup. A spherical resonator made of Pyrex of 60 mm in diameter and with a resonance frequency of approximately 28.3 kHz was filled with distilled, 0.45-μm-filtered, and partially degassed water. The experiments were conducted at a controlled temperature of 22.3 °C (295.3 K) and a room pressure of 0.92 bar (our laboratory is 764 m above sea level) in a closed system (no free surfaces were present).

We add to the completely degassed water a controlled amount of air. A closed system is needed in order to have the concentration of the dissolved gases constant in time during the experiments. In practice we achieved the target air concentration using a magnetic stirrer to ensure adequate mixing. After this, we let the fluid rest for at least 1 h in order to reach thermodynamic equilibrium. We also computed the following two corrections: one to account for the water vapor pressure present in the mixture on top of the water surface and the other for the slight temperature difference between

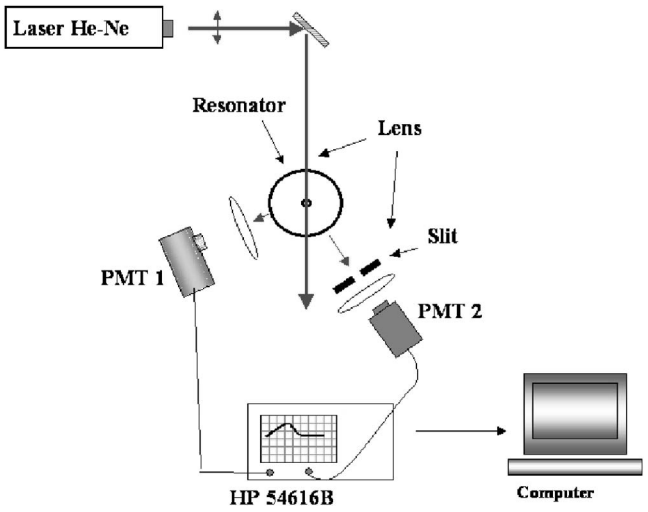

FIG. 1. Schematics of the experimental setup.

the water temperature during gas dissolution and the temperature in the resonator.

We developed a closed loop liquid temperature control system that was able to set the temperature to a certain value with an uncertainty of 100 mK and more importantly with a short term (1 h) stability better than 50 mK. This very low temperature fluctuation was required to perform the dissolution limit experiment described below.

The primary measured variable was the absolute value of $R(t)$ with the air concentration and acoustic pressure as parameters.

We determined experimentally the absolute value of the bubble radius using a two-photodetector technique and Mie scattering [22]. One of the detectors is located for side scattering with a large collection angle. The light intensity is proportional under this arrangement to the square of the bubble radius. The constant of proportionality is obtained with another detector that is located near forward scattering using a very small collecting angle. The signal of this detector reflects "resonances" that are computed using Mie scattering. From the comparison between these computations and the two-detector measurement technique we obtain a robust estimation technique to determine the absolute value of the bubble radius without the need of a RPE fit.

We illuminated the bubble with a HeNe laser of 30 mW and horizontal polarization. We used one photodetector (Brand Oriel model 77340) as the detector that produces a signal proportional to the squared bubble radius at an angle of 70° with respect to forward scattering and with a collecting angle of 60°. For the absolute value of the radius we used a second photodetector (Brand Hamamatsu, model H957) located at an angle of 21.4° with respect to forward scattering and with a collecting angle of 4.04°. The experimental uncertainty in the radius is controlled by the geometrical uncertainties.

An $R(t)$ curve is obtained from 50 single shot traces taken every 4 s approximately. The 50 traces had a scattering in the time of collapse of approximately 200 ns. This scattering depends on the phase space region under investigation and

it is smallest in the SL region. We selected the traces that had a scattering in time of collapse of 30 ns or less. We averaged these selected traces and we assigned to the resulting curve an error equal to the standard deviation at a given time divided by the square root of the number of averaged traces. This procedure underestimates the experimental error.

The two photodetector traces were digitized at a sampling rate of 100×10^6 samples/s (points separated by 10 ns in time). We acquired 5000 points for each trace and we used for the data analysis approximately 3000 points.

In order to obtain the absolute acoustic pressure we performed the following procedure. For a given gas concentration there is a minimum acoustic pressure that is able to keep the bubble in diffusive equilibrium (dissolution limit). This point in a constant concentration equilibrium curve corresponds also to a certain value for the ambient radius and acoustic pressure (P_a^*,R_0^*). This point can be achieved experimentally only if the shape instability curve is above (P_a^*,R_0^*). If the shape instability is below $(P_a{}^*,R_0^*)$ for a given P_a, the value of R_0 is given by this shape instability curve [17]. When this occurs the minimum acoustic pressure point that can be obtained experimentally is given by the intersection of the shape instability and the diffusive stability curve, and this point becomes the dissolution limit.

We took advantage of this fact to perform a robust calibration of the acoustic pressure. We slowly reduced the acoustic pressure right before the point where the bubble disappeared. We observed the bubble using a charge-coupled device camera connected to a TV monitor and the scattered light on the oscilloscope. In the case of dissolution we observed that the light scattered to the photodetectors by the bubble diminished with time (due to the reduction in size) and eventually was invisible. This process was relatively slow with a time scale compatible with mass diffusion. We observed that the acoustic pressure that corresponded to the dissolution limit for a given absolute gas concentration depended on the liquid temperature. For this reason we built a system able to control the liquid temperature with a very good short term stability. In these conditions, the reproducibility in the acoustic pressure for the dissolution limit was better than 0.2%. The stability of this bubble was comparable to the stability of SL bubbles and much better than non-SL bubbles present in other regions of the (P_a,R_0) parameter space. We could measure the radius temporal evolution for bubbles that corresponded to an acoustic pressure 0.2% higher than the dissolution limit. For a fixed gas concentration the value of P_a in the dissolution limit is unique. This value of P_a must satisfy two conditions: on one hand it must fit the measured temporal evolution for the bubble radius and on the other hand it must correspond to the intersection of the shape instability and diffusion equilibrium curves computed by the model.

In summary, the procedure to obtain the absolute acoustic pressure is as follows.

(1) For a fixed gas concentration (c_∞/c_0) we computed the (P_a,R_0) point that corresponded to the intersection between the shape instability and the diffusion equilibrium curves using our model. We computed the temporal evolution $R(t)$ for this point (P_a,R_0). This represents our model prediction.

(2) We used two-detector light scattering data and Mie scattering with resonances, that is, absolute calibration of the radius evolution. This represents our experimental result that was obtained without the use of the RPE.

(3) We compared this technique (two photodetectors) with one photodetector and a RPE fit. The agreement was excellent with the model presented in this paper.

III. MODEL

The temporal evolution of the radius of a SBSL bubble can be described by the Rayleigh-Plesset equation [9]

$$\left(1-\frac{R}{c_L}+\frac{m}{c_L\rho_{L,i}}\right)RR+\frac{3}{2}R^2\left(1-\frac{R}{3c_L}+\frac{2m}{3c_L\rho_{L,i}}\right)=\frac{1}{\rho_{L,i}}\left(1\frac{R}{c_L}\right)\left[p_B-p_s\left(t\frac{R}{c_L}\right)-p_\infty\right]+\frac{mR}{\rho_{L,i}}\left(1-\frac{R}{c_L}+\frac{m}{c_L\rho_{L,i}}\right)$$
$$+\frac{m}{\rho_{L,i}}\left(R-\frac{m}{2\rho_{L,i}}+\frac{mR}{2c_L\rho_{L,i}}\right)+\frac{R}{c_L\rho_{L,\infty}}\frac{dp_B}{dt} \quad (1)$$

where the liquid viscosity, liquid compressibility, and condensation-evaporation effects are taken into account.

In Eq. (1) c_L is the liquid speed of sound at infinity, m is the evaporation net flux, $\rho_{L,i}$ $(\rho_{L,\infty})$ is the liquid density at the bubble surface (at infinity), $p_B(t)$ is the liquid pressure at the bubble surface, and p_∞ is the ambient pressure at infinity. $p_s(t)$ is the part of the ambient pressure that changes with time. For the cases studied in this work $p_s(t)$ is the ultrasonic pressure:

$$p_s(t)=P_a\sin(wt-\phi) \quad (2)$$

where P_a is the ultrasound wave amplitude, w is the angular frequency $(2\pi f=w)$, and ϕ is the phase (equal to π).

The evaporation net flux is computed using [9]

$$m=m_{\mathrm{eva}}-m_{\mathrm{con}}, \quad (3)$$

$$m_{\mathrm{eva}} = \frac{\alpha_M}{\sqrt{2\pi R_v}} \frac{p_{\mathrm{vap}}}{T_{L,i}^{1/2}}, \tag{4}$$

$$m_{\mathrm{con}} = \frac{\alpha_M}{\sqrt{2\pi R_v}} \frac{\Gamma p_v}{T_B^{1/2}}, \tag{5}$$

where R_v is the gas constant for the vapor in J/kg K, p_{vap} is the saturation vapor pressure evaluated at the liquid interphase temperature $T_{L,i}$, and p_v is the actual vapor pressure:

$$p_v = \frac{n_v}{n_t} p_t, \tag{6}$$

where Γ is given by the following expression [9]:

$$\Gamma = \exp(-\Omega^2) - \Omega\sqrt{\pi}\left(1 - \frac{2}{\sqrt{\pi}}\int_0^{\Omega} \exp(-x^2)dx\right) \tag{7}$$

and Ω is given by

$$\Omega = \frac{m}{p_v}\left(\frac{R_v T}{2}\right)^{1/2}. \tag{8}$$

α_M is the accommodation coefficient for condensation and evaporation. We take this value to be 0.1. Values smaller than 0.1 seem to be unrealistic based on published results. Also our calculations show that the results are very insensitive to the accommodation coefficient for values in the [0.1,1] range.

Using gas kinetic theory the temperature jump at the bubble surface is given by [23]

$$T_B = T_{L,i} + \Delta T \tag{9}$$

and the temperature jump at the bubble wall is given by [23]

$$\Delta T = -\frac{1}{2k_B n'}\left(\frac{\pi m}{2k_B T_B}\right)^{1/2} \frac{2 - a'\alpha_E}{\alpha_E} q'' \Big|_{r=R} \tag{10}$$

where k_B is the Boltzmann constant, T_B is the gas-vapor mixture temperature at the bubble wall, n' is the total number of particles (gas and vapor) per unit volume inside the bubble, m is the mean molecule mass, α_E is the thermal accommodation coefficient $\alpha_E = 1$, $a' = 0.827$ is a constant that depends on the gas inside the bubble [9], and $q''|_{r=R}/k$ is the gas temperature gradient at the bubble wall. This temperature gradient is computed from the temperature solutions obtained with the collocation point results in the gas or the thermal boundary layer results, depending which model is being used. The thermal conductivity k is computed based on the thermal conductivity of each gas species weighted with the corresponding molar fractions.

The pressure $p_B(t)$ is related to the pressure inside the bubble by the following expression [12,9]:

$$p_B(t) = p_t(t) - \frac{2\sigma}{R} - \frac{4\mu}{R}\left(R - \frac{m}{\rho_{L,i}}\right) - m^2\left(\frac{1}{\rho_{L,i}} - \frac{1}{\rho_t}\right) \tag{11}$$

where σ is the surface tension, μ is the liquid viscosity, and ρ_t is the total density inside the bubble.

If the continuity equation (i.e., mass conservation) is multiplied by $C_p T$ and added to the energy conservation equation we obtain

$$\frac{D}{Dt}(C_p \rho T) + \frac{T}{\rho}\left(\frac{\partial \rho}{\partial T}\right)_p \frac{dp_t}{dt} + C_p \rho T \nabla \cdot u = \nabla(k \nabla T). \tag{12}$$

We notice that the following analysis is valid for temperatures that are obtained in the bubble such that the mixture present in the bubble can be considered as an ideal gas. Using this approximation we have that $C_p T\rho = \gamma p_t/(\gamma - 1)$; therefore $(T/\rho)(\partial\rho/\partial T)_p = -1$, where γ is the ratio between the specific heat at constant pressure and the specific heat at constant volume. Combining this result with the assumption that the gas has spatially uniform properties one obtains

$$\frac{p_t}{\gamma p_t} + \nabla \cdot \{u - [(\gamma - 1)/\gamma p_t] k \nabla T\} = 0. \tag{13}$$

The problem under consideration has spherical symmetry. We integrated analytically Eq. (13) obtaining the following result for the velocity field inside the bubble:

$$u = \frac{1}{\gamma p_t}\left((\gamma - 1)k\frac{\partial T}{\partial r} - \frac{1}{3} r p_t\right). \tag{14}$$

We rewrite the energy equation using Eq. (14) and the ideal gas approximation, obtaining

$$\frac{\gamma}{\gamma - 1}\frac{p_t}{T}\left(\frac{\partial T}{\partial t} + u\frac{\partial T}{\partial r}\right) = p_t + \frac{1}{r^2}\frac{\partial}{\partial r}\left(kr^2\frac{\partial T}{\partial r}\right). \tag{15}$$

With the ideal gas approximation the temporal derivative of the bubble pressure is given by

$$p_t = \frac{R_g T}{NaV}\frac{dn_t}{dt} + \frac{n_t R_g}{NaV}\frac{dT}{dt} - \frac{n_t R_g T}{NaV^2} 4\pi R^2 R, \tag{16}$$

where $dn_t/dt = n_v$, due to the fact that the number of noncondensable gas molecules is constant. The temporal derivative of the temperature is obtained from the energy equation in Eq. (16).

IV. CHEMICAL KINETICS

The chemical kinetic model presented in this work is based on [12,9,13] and developed along the lines of Egolfopoulos and Law [24] to describe the molecular decomposition of the water vapor molecules inside the bubble upon collision with an inert gas. It includes the elementary reactions between stable species and free radicals for the system.

The kinetic model is applied to each dissociable species of an air bubble such as N_2, O_2, and water vapor molecules. However, the phenomenon of dissociation in H_2O vapor molecules can be neglected because the number of molecules of this species changes mainly by condensation or evaporation [9]. In the calculations described here it is also possible to neglect water vapor molecules as the collision partner or the third body in a three-body reaction. When the temperatures reached inside the bubble during collapse are suffi-

TABLE I. Chemical kinetic model used for the dissociation of N_2 and O_2. Values from [25].

System	A_b [m^3/mol s)	β_b[1]	C_b(K)
O_2 in an Ar bath	1.81×10^{12}	−1.0	59420
O_2 in an O_2 bath	1.07×10^{13}	−1.0	59420
O_2 in an N_2 bath	3.39×10^{12}	−1.0	59420
N_2 in an Ar bath	1.90×10^{11}	−0.5	112563[a]
N_2 in an O_2 bath		−0.5	112563[a]
N_2 in an N_2 bath	4.80×10^{11}	−0.5	112563[a]

[a]From [26].

ciently high to produce dissociation, the amount of vapor molecules is very small compared to the amount of noncondensable molecules, so we neglect the water vapor chemical reactions [9].

We consider a general reaction

$$\sum_i a_i A_i \rightarrow \sum_j b_j B_j \tag{17}$$

where a_i and b_j are the number of molecules contributing to one reaction of the species A_i and B_j, respectively. The forward reaction rate per unit volume and unit time is calculated from [12,9,13]:

$$r_f = \prod_i k_{fi}[A_i]^{a_i} \tag{18}$$

where

$$k_{fi} = A_{fi} T^{\beta_{fi}} \exp(-C_{fi}/T). \tag{19}$$

The concentration of the species A_i ($[A_i]$) is expressed in moles per m^3; thus A_{fi} is expressed in m^3/mol s for a two-body reaction, β_{fi} is dimensionless, and C_{fi} is in K and is related to the reaction enthalpy change. The backward reaction is calculated in a similar manner.

The change in the number of each species (n_α) with time due to chemical reactions is given by

$$\frac{dn_\alpha}{dt} = VN_a\left(\sum \text{production} - \sum \text{destruction}\right) \tag{20}$$

where the first sum contains the contribution of all reaction producing α, and the second one contains that of all reactions consuming α.

When the gas inside the bubble is hot enough (upon collapse), dissociation of N_2 and O_2 can be significant. The dissociated nitrogen and oxygen will undergo chemical reactions, whose products are very soluble in water and are expelled from the bubble [27]. Thus there is no possibility of recombination for the products; therefore, the net production is zero.

The change in the number of oxygen molecules is given by

$$\begin{aligned}\frac{dn_{O_2}}{dt} = &-\frac{A_{O_2\text{-Ar}}}{NaV} T^{\beta_{O_2-Ar}} \exp(-C_{O_2\text{-Ar}}/T) n_{O_2} n_{Ar} \\ &-\frac{A_{O_2\text{-}O_2}}{NaV} T^{\beta_{O_2\text{-}O_2}} \exp(-C_{O_2\text{-}O_2}/T) n_{O_2} n_{O_2} \\ &-\frac{A_{O_2\text{-}N_2}}{NaV} T^{\beta_{O_2\text{-}N_2}} \exp(-C_{O_2\text{-}N_2}/T) n_{O_2} n_{N_2}\end{aligned} \tag{21}$$

where the O_2 can be consumed if it collides with a molecule of Ar, N_2, or O_2.

A similar equation is used for the change in the number of N_2 molecules. Table I gives the constants needed to compute them for Oxygen concentration and Nitrogen concentration.

V. DIFFUSIVE STABILITY

The number of molecules for noncondensable gases in the bubble can also change because of diffusion through the bubble surface. What follows is the mathematical description of this effect [17].

Assuming spherical symmetry, the mass concentration of gas $c(r,t)$ dissolved in the liquid at distance $r > R(t)$ from the center of the bubble obeys the advection-diffusion equation

$$\frac{\partial C}{\partial t} + u \cdot \nabla C = -D\nabla^2 C. \tag{22}$$

Assuming Henry's law as a boundary condition at the bubble wall,

$$C(R(t),t) = C_0 p(R(t),t)/p_0. \tag{23}$$

The main idea is to treat the diffusive PDE by the method of separation of time scales [28,29]: the concentration field is split into an oscillatory part changing on the fast time scale T of the driving field, and a smooth part changing on a slow diffusive time scale $T_D \gg T$.

The main result of [28] is that in the asymptotic limit, the smooth profile converges to

$$C_{\text{smooth}}(h) = C_\infty + \left(C_0 \frac{\langle p_{\text{gas}} \rangle_4}{p_0} - C_\infty \right) \times \left(1 - \frac{\int_0^h \frac{dh'}{\langle [3h' + R^3(t)]^{4/3} \rangle_0}}{\int_0^\infty \frac{dh'}{\langle [3h' + R^3(t)]^{4/3} \rangle_0}} \right) \tag{24}$$

where the weighted time averages are given by

$$\langle f(t) \rangle_i = \frac{\int_0^T f(t) R^i(t) dt}{\int_0^T R^i(t) dt}.$$

The concentration gradient at the moving boundary gives the mass loss or gain of the bubble:

$$m = 4\pi R^2 \left. \frac{\partial C}{\partial r} \right|_{r=R(t)}. \tag{25}$$

Using Eqs. (24) and (25) we can determine the time evolution of the number of molecules of a given species due to diffusion. For example, the change in the number of O_2 molecules with time due to diffusion is given by

$$\frac{dn_{O_2}}{dt} = - \frac{4\pi C_{0O_2} D_{O_2} N_A R^4}{\langle R^4 \rangle_0 I M_{O_2}} \left[\frac{n_{O_2}}{n_t} \frac{\langle p_g \rangle_4}{P_\infty} - \left(\frac{C_\infty}{C_{0O_2}} \right) \right]. \tag{26}$$

The integral I can be calculated numerically [17]:

$$I = \int_0^\infty \frac{dh'}{\langle [3h' + R^3(t)]^{4/3} \rangle_0} \approx \frac{a}{R_{max}} + \frac{1-a}{R_0} + (3h_{max})^{-1/3} \tag{27}$$

with $a = 0.9$.

The ambient radius is in equilibrium if the net variation in the number of each species, in an acoustical cycle, is equal to zero:

$$\int_T \left. \frac{dn_\alpha}{dt} \right|_{\text{dissociation}} + \int_T \left. \frac{dn_\alpha}{dt} \right|_{\text{diffusion}} = 0. \tag{28}$$

VI. RESULTS

We numerically solved the previous system of equations (1)–(11) using an adaptive Runge-Kutta solver. We determined that integrating the system of equations during eight cycles resulted in a solution insensitive to initial conditions. The last cycle was taken as the solution for the system in the limit $t \to \infty$. Figure 2(b) shows the absolute radius as a function of time obtained with the two-detector technique for a point of minimum acoustic pressure and an air concentration of 0.15. The solid curve represents the numerical results for the predicted point for minimum acoustic pressure ($P_a = 0.925$ bar, $R_0 = 8.09$ μm). The bottom curve (labeled Experimental variance) gives an indication of the dispersion in the experimental data

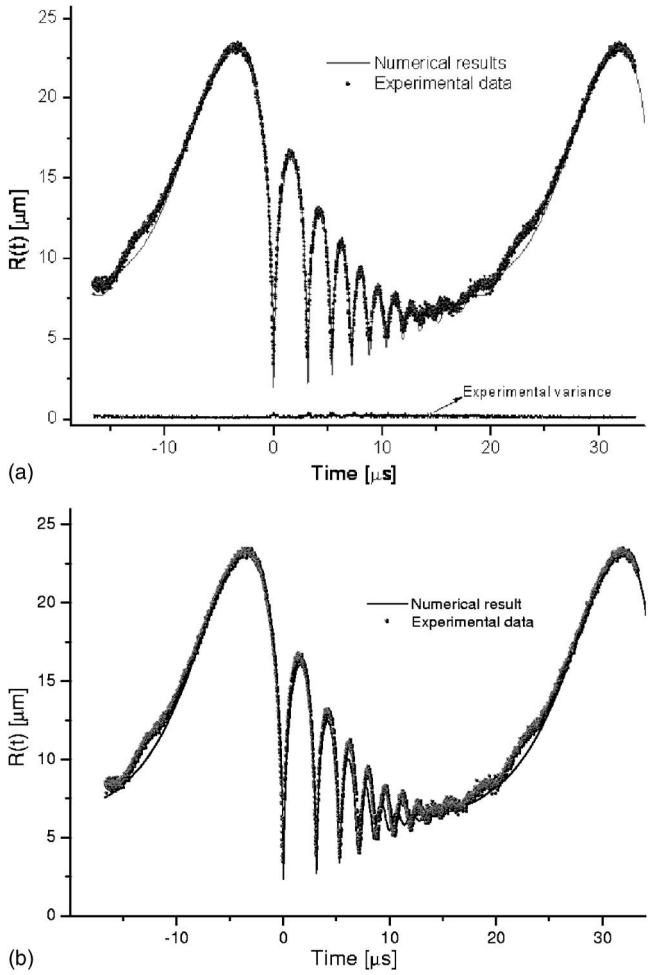

FIG. 2. Temporal evolution of a bubble radius for $P_a = 0.925$ bar, $c = 0.15$ (resulting in a $R_0 = 8.09$ μm) corresponding to the dissolution limit. The experiments are results with the use of two detectors (absolute measurement). (a) Solid line shows our numerical results. The bottom curve represents the experimental error as a function of time. (b) Solid line represents numerical fitting using heat transfer model.

We observed that the agreement between the experimental results and the model is almost perfect except for a small region in the final stages of the rebounds and the beginning of the expansion phase. We believe that this "bump" in the light scattering data is due to the fact that the bubble is nonspherical as a consequence of a shape instability. We removed the data points corresponding to the bump for the data analysis. We observed the presence of this bump for time intervals of the order of minutes.

Figure 2 shows the temporal evolution of the same bubble as in Fig. 2(a) where the solid curve represents a numerical fitting using the heat transfer model (thermal boundary layer) proposed by Toegel *et al.* [14] and Toegel and Lohse [13].

Toegel's [13] approach to computing the gas temperature distribution involves the use of a boundary layer thickness. That is, a single value for the thickness is used for a given time. On the other hand the Hao and Prosperetti approach

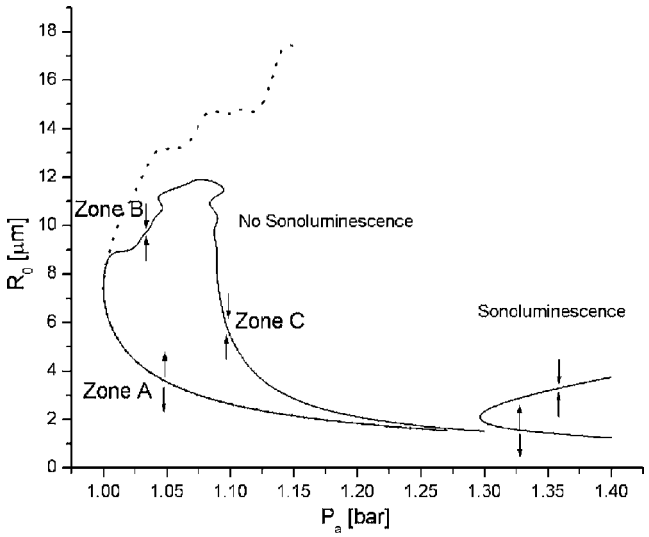

FIG. 3. Phase plane for a concentration of $c=0.07$.

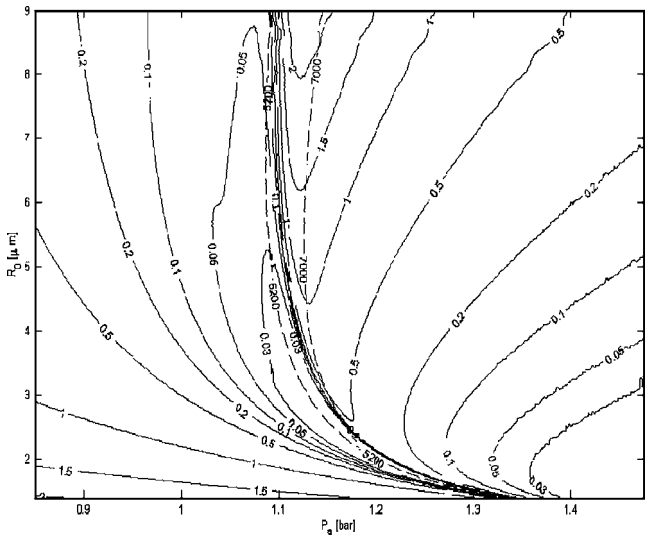

FIG. 4. Phase plane for several concentrations.

solves the partial differential equation for the spatial temperature dependence using a collocation method that reduces the partial differential equation to a set of ordinary differential equations. Both methods produce similar results for moderate and high acoustic pressures. However, for low acoustic pressures the Hao and Prosperetti approach is superior. An accurate description of the spatial and temporal evolution of the temperature is very important to model the low acoustic pressure bubbles during the rebounds. We followed Hao and Prosperetti in our model. In this way we retain the accuracy of a PDE calculation and at the same time we keep the computational time low.

Despite the fact that the fits in Figs. 2(a) and 2(b) differ significantly in the rebounds, the curves of isoconcentration do not present significant differences in the $(R_0$-$P_a)$ phase diagram. The reason is that the concentration depends on the temporal evolution of the radius to the fourth power. Therefore the contribution to the isoconcentration curves is mainly determined by the maximum radius. The fits near the maximum radius are very good in both figures and the differences in the rebounds do not reflect on the isoconcentration curves.

To give more credence to the P_a value we performed a consistency check. The acoustic pressure is expected to be proportional to a driving quantity in the experiment. We obtained that the fitted acoustic pressure from the experimental radius temporal evolution shows a linear relationship with the external microphone reading (root mean square volts with a 1 MΩ load). At low acoustic pressures this relationship closely follows a straight line. This indicates that the fit is very good in this region (low scatter) and also indicates that the dissolution limit is an adequate point to fit. As we increase the acoustic pressure the scatter increases and becomes relatively large in the dissociation regime. Finally for high acoustic pressures (the SL regime) the scatter tends to diminish again. This result gives us confidence in our parameter (in particular P_a) estimation strategy.

Figure 3 shows a phase diagram (R_0, P_a) corresponding to $c_\infty/c_0=0.07$. The dotted line shows the phase diagram when we consider only diffusive equilibrium. In this case a negative slope corresponds to nonstable equilibrium. The solid line shows the phase diagram when both mass diffusion and dissociation are considered. For this case we may have stable equilibrium still when the slope of the threshold curve is negative.

The stability curve corresponding to diffusion is very similar to the curve that we obtained considering dissociation in zone *A*. This is due to the fact that low temperatures are achieved during collapse and therefore the dissociation effects are negligible. On the other hand in zone *B* dissociation effects are dominant. A negative slope in zone *B* corresponds to the region of parameter space where the amount of N_2 that is lost due to dissociation is important.

For the same concentration of 0.07 there is another R_0-P_a curve that corresponds to sonoluminescence (SBSL). The resulting curve is identical to the curve obtained when we assume that only Ar is dissolved in water with a molar fraction of 0.0007 (1% of 0.07). This is a consequence of almost complete dissociation of N_2 and O_2.

Figure 4 shows a family of stability curves with the air concentration in the liquid as a parameter. If the air concentration is high enough there is a boundary curve for the diffusive equilibrium. For the range of R_0 shown in Fig. 4 the curve has a negative slope. On top of this curve there is another curve that is stable even though the slope is negative where the dissociation effects are important. If we have a bubble in this dissociation region and we increase the acoustic pressure, the ambient radius will decrease, up to the diffusive equilibrium curve that has almost pure Ar. As we increase the acoustic pressure the ambient radius increases, following the path of the SL curve (which is almost coincident with the diffusive equilibrium for pure Ar).

Figure 5 shows the molar fractions of N_2, O_2, Ar, and vapor H_2O as a function of P_a for an R_0 of 7 μm, at the moment of bubble collapse. The behavior is similar for other R_0's. For low P_a the molar fractions are equal to the air molar fractions. As we increase P_a first the O_2 dissociates completely and then the same happens with the N_2. The amount of H_2O is almost negligible.

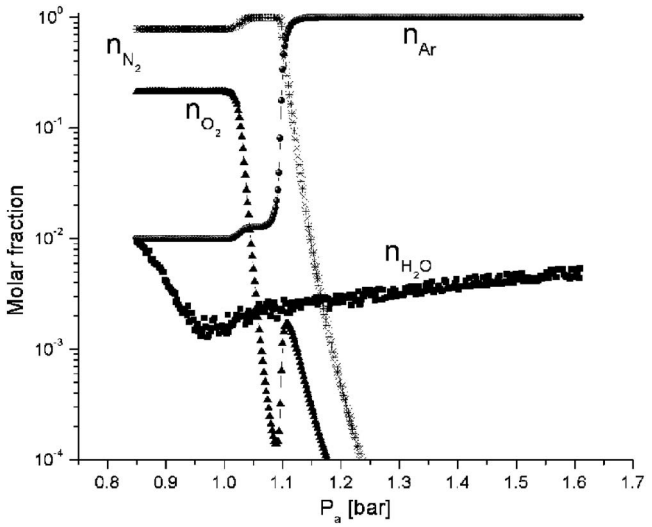

FIG. 5. N_2, O_2, H_2O vapor, and Ar molar fractions during bubble collapse. Equilibrium points. $R_0=7$ μm.

Figures 6(a)–6(c) show the molar fractions of the different species for equilibrium states as a function of R_0 and P_a. These molar fraction values are obtained from the smooth solutions and therefore a cycle is characterized by a single value. What follows is a description of how Fig. 6(a) was obtained. Figures 6(b) and 6(c) were similarly obtained. For a given pair (R_0, P_a) the model was solved as we described before. This particular solution will be compatible with a value of air concentration in water $c=c_\infty/c_0$. As a result of the calculation we also obtain the molar fraction of O_2 inside the bubble that corresponds to R_0 and P_a(and c_∞/c_0). The equilibrium state does not necessarily correspond to a stable bubble. The stability information is contained in Fig. 4. If a point (R_0, P_a) belongs to a zone A of the corresponding c_∞/c_0 curve the bubble will be unstable. On the other hand, if a point (R_0, P_a) belongs to a zone B or SL (positive slope) of the corresponding c_∞/c_0 curve the bubble will be stable and in the long run the O_2 molar fraction will be the one given in Fig. 6(a).

In Fig. 6(a) we can see that for ambient radius $R_0=7$ μm there are two distinct regions. For acoustic pressures $P_a<1$ bar the O_2 molar fraction inside the bubble is equal to 0.21 (the normal O_2 concentration in air), indicating that there are practically no dissociation effects either in O_2 or in N_2. For acoustic pressures $P_a>1$ bar the O_2 molar fraction inside the bubble decreases rapidly (to 0), indicating that the temperature reached in the bubble is enough to dissociate O_2. Moreover the result indicates that the net gain in O_2 due to mass diffusion in one cycle is dissociated due to the high temperatures reached in the bubble during collapse.

For an R_0 of 7 μm, the dissociation of O_2 starts to be significant at a P_a of 1.016 bar (significant means that the O_2 molar fraction inside the bubble changes from 0.21 to 0.20). The maximum temperature inside the bubble reaches $T_{max}=2760$ K. For the same R_0 of 7 μm at an acoustic pressure P_a of 1.05 bar the dissociation of O_2 is practically complete. The maximum bubble temperature in this case is $T_{max}=3869$ K. For acoustic pressures higher than 1.05 bar

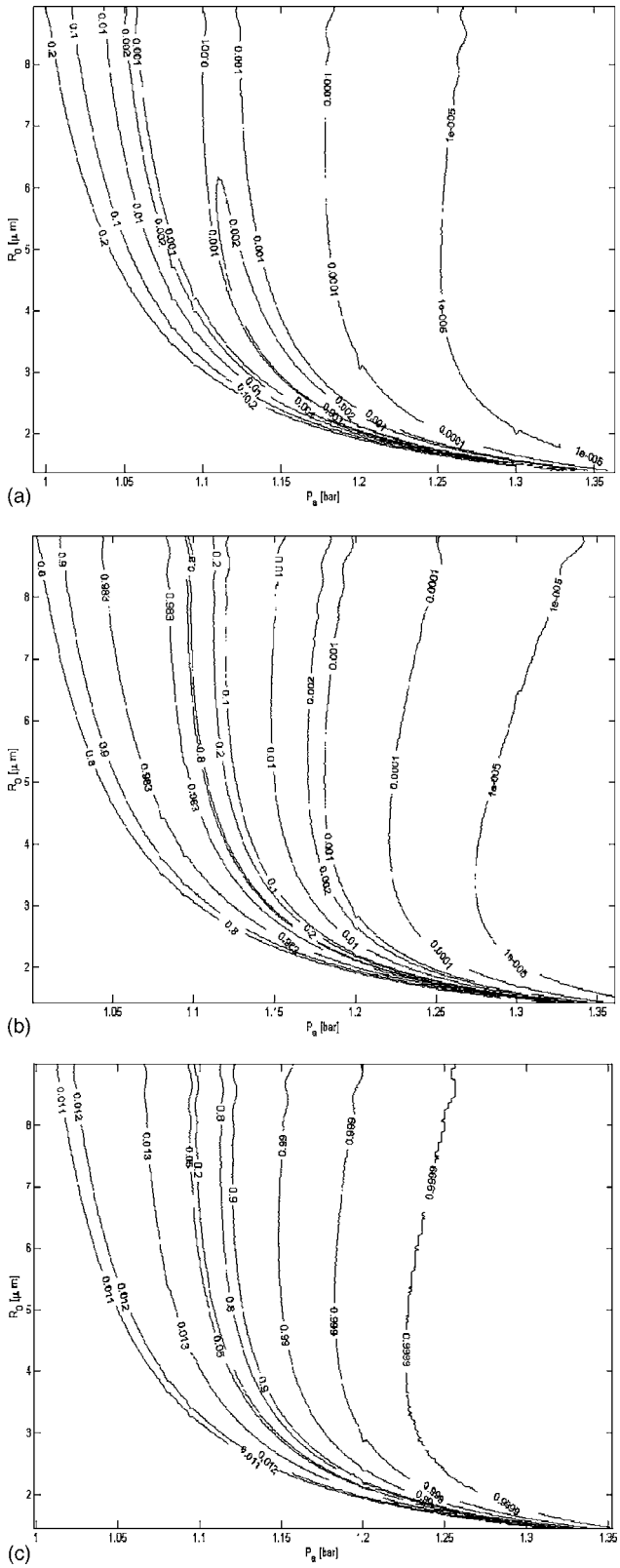

FIG. 6. (a) O_2, (b) N_2, and (c) Ar molar fractions. Equilibrium points.

the O_2 dissociation for all practical purposes is complete. Because of the assumption that monotomic oxygen (O) is completely soluble in water for pressures higher than 1.05 bar there is no O_2 or O present in the bubble if $R_0=7$ μm. In

Fig. 6(a) there is a narrow region where the O_2 molar fraction has values between 0.21 and 0. On the left of this narrow region the O_2 molar fraction is almost constant and equal to the standard concentration of O_2 in air (that is 0.21). On the right of this narrow region there is practically no O_2 (that is, zero molar fraction).

Figure 6(b) shows the N_2 molar fraction as a function of R_0 and P_a. There is a narrow region where the N_2 molar fraction changes from the standard molar fraction in air (that is, 0.78) to a value of 0.99. This region coincides in the (R_0, P_a) phase plane with the narrow region described in Fig. 6(a). This can be understood as follows. On the left of this transition region the maximum temperatures attained by the bubble are not sufficient to dissociate O_2 or N_2 (Ar does not dissociate because is monatomic). In this region of parameter space the molar fractions of all species are the standard values for the different species (0.78 for N_2, 0.21 for O_2, 0.01 for Ar). On the right of the narrow region described in Fig. 6(a) the O_2 is completely dissociated (molar fraction equal to 0), the N_2 concentration increases to 0.99, and the Ar concentration remains approximately equal to 0.01. However, in Fig. 6(b) there is another transition for higher acoustic pressures due to the N_2 dissociation.

When N_2 dissociates, its molar fraction changes from 0.99 to 0. For these high temperatures (corresponding to high acoustic pressures) the Ar molar fraction changes from 0.01 to 1. For an ambient radius of $R_0=6.5$ μm N_2 dissociation begins for an acoustic pressure $P_a=1.095$. The maximum temperature during compression is 5600 K in this case. For an ambient radius of $R_0=6.4$ μm N_2 dissociation is complete for an acoustic pressure $P_a=1.13$. In this case the maximum temperature during compression is 6990 K.

Figure 6(c) shows the molar concentration of Ar as a function of R_0 and P_a. There is no dissociation in Ar. The changes in the Ar molar fraction reflect the dissociation and diffusion processes in N_2 and O_2. Figure 6(c) shows that the dissociation of O_2 has practically no effect on the molar fraction of Ar (which remains equal to the standard value of 0.01). However, the dissociation of N_2 has an impact on the Ar molar fraction. As the N_2 molar fraction changes from 0.99 to 0 the Ar molar fraction changes from 0.01 to 1. This is a natural consequence of the fact that in this region there is no O_2 present and that all the molar fractions add up to 1.

We note that even though in the SL region the bubble during collapse is practically all Ar (the water content is negligible) it is not the same to consider water with pure Ar dissolved and water with air dissolved at the same concentration of Ar. In other words if we have a system in which the water is in thermodynamic equilibrium with an atmosphere of 100 mbar of air (which contains a 1 mbar partial pressure of Ar) this system will not behave identically to another system with an atmosphere of pure Ar and pressure 1 mbar. The reason for the difference is that in the air-water SL system in each acoustic cycle a certain mass of N_2 and a certain mass of O_2 enter the bubble. The N_2 and O_2 are completely dissociated during collapse but this reaction is endothermic and reduces the maximum temperature that is attained. On the other hand when pure Ar is dissolved in water there is no dissociation and therefore higher temperatures are obtained. Hence it is not strictly correct to compute maximum temperatures in SL considering only noble gases in the bubble when there are carrier gases such as O_2 or N_2 present in the liquid. Figure 7 shows the experimental and numerical phase diagrams for different air concentrations in water. Each experimental point represents the acoustic pressure amplitude and the ambient radius obtained from fitting the experimentally obtained $R(t)$ curves using the numerical model proposed in this work.

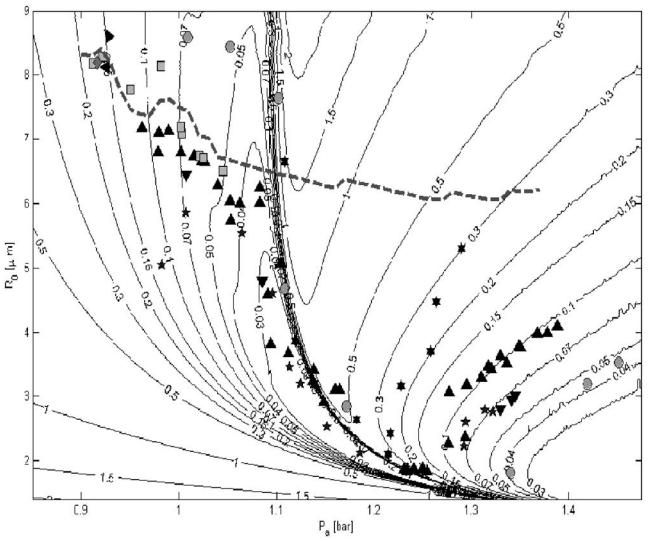

FIG. 7. Comparison between experiments and numerical results in the forced bubble phase plane. The dashed line curve corresponds to the $n=2$ shape instability. The circles, down triangles, up triangles, and stars correspond to the concentrations 0.05, 0.064, 0.12, and 0.2. The leftmost and rightmost filled triangles correspond to the dissolution points for concentrations 0.064 and 0.15.

For low gas concentrations the data were not obtained from a single bubble. We could not make the transition from non-SL to SL for this low gas concentration. The data were taken by seeding one bubble with a low acoustic pressure for the non-SL bubble and seeding another bubble at a high acoustic pressure for the SL bubble.

The data in the SL region present an excellent correspondence (between non-SL and SL data and also between experimental and measured concentrations) with the minimum values of non-SL bubbles (dissolution limit). This is true except for $c=0.05$ which has a dissolution limit at $c=0.07$. This concentration also presents the anomaly that three experimental points are above the shape instability.

There is a qualitative and quantitative agreement between experimental and theoretical points in the shape instability of order $n=2$. The excellent agreement between experiments and calculations in the region where N_2 is completely dissociated makes us believe that the model is capable of accurately determining the maximum temperatures during collapse.

VII. CONCLUSIONS

In this work we present a model that takes into account all the physics that are relevant to describe the temporal evolution of an acoustic bubble from very low acoustic pressures

(dissolution limit) all the way up to high acoustic pressures (extinction limit).

We also present experiments that cover the phase diagram domain (R_0, P_a) from dissolution to extinction and from low to high air concentrations. These experiments produced results of unprecedented accuracy. When phase diagram experiments and calculations are compared we find the agreement to be very good. When we compare radius temporal evolutions the agreement is excellent throughout the phase diagram. The rebounds are captured by our model without any fitting parameters.

The dissolution point is used to obtain the absolute value of the radial evolution due to its high stability and the fact that after we fix two parameters (c and P_a for example) the third (R_0) becomes univocally determined and it is used to obtain $R(t)$ with high precision.

The upper boundary of the phase diagram shows a good agreement between the experimental points and a calculation of the shape instabilities obtained following Hao and Prosperetti but without taking into account the vorticity in the liquid. However, we measured several points that are above the computed shape instability curve.

For a given amount of air dissolved in water we found that the concentrations and acoustic pressures obtained with the fit are consistent with the model in the whole range of measured pressures.

ACKNOWLEDGMENTS

We acknowledge the technical support of Sebastian Eckardt and Daniel Mateos. G.F.P. is financed by Anpcyt/Secyt and R.U. by CONICET/CNEA. The partial support of Foncyt/Anpcyt/Secyt through Grant No. PICT 12-09848 is gratefully appreciated.

[1] M. P. Brenner, S. Hilgenfeldt, and D. Lohse, Rev. Mod. Phys. **74**, 425 (2002).
[2] C. C. Wu and P. H. Roberts, Phys. Rev. Lett. **70**, 3424 (1993).
[3] W. C. Moss, D. B. Clarke, and J. W. White, Phys. Fluids **6**, 2979 (1994).
[4] B. D. Storey and A. J. Szeri, J. Fluid Mech. **396**, 203 (2000).
[5] B. D. Storey, Phys. Rev. E **64**, 017301 (2001).
[6] J. B. Keller and M. J. Miksis, J. Acoust. Soc. Am. **68**, 628 (1980).
[7] L. Rayleigh, Philos. Mag. **34**, 94 (1917).
[8] M. Plesset, J. Appl. Mech. **16**, 277 (1949).
[9] K. Yasui, Phys. Rev. E **56**, 6750 (1998).
[10] Y. Hao and A. Prosperetti, Phys. Fluids **11**, 1309 (1999).
[11] R. Toegel, B. Gompf, R. Pecha, and D. Lohse, Phys. Rev. Lett. **85**, 3165 (2000).
[12] V. Kamath, A. Prosperetti, and F. Egolfopoulos, J. Acoust. Soc. Am. **94**, 248 (1993).
[13] R. Toegel and D. Lohse, J. Chem. Phys. **118**, 1863 (2003).
[14] R. I. Nigmatulin, N. S. Khabeev, and F. B. Nagiev, Int. J. Heat Mass Transfer **24**, 1033 (1981).
[15] R. Toegel , B. Gompf, R. Pecha, and D. Lohse, Phys. Rev. Lett. **85**, 3165 (2000).
[16] V. Kamath and A. Prosperetti, J. Acoust. Soc. Am. **85**, 1538 (1989).
[17] S. Hilgenfeldt, D. Lohse, and M. Brenner, Phys. Fluids **8**, 2808 (1996).
[18] R. G. Holt and D. F. Gaitan, Phys. Rev. Lett. **77**, 3791 (1996).
[19] B. P. Barber, S. J. Putterman, Phys. Rev. Lett. **69**, 3839 (1992).
[20] J. A. Ketterling and R. E. Apfel, Phys. Rev. E **61**, 3832 (2000).
[21] A. Eller and L. A. Crum, J. Acoust. Soc. Am. **47**, 772 (1970).
[22] G. A. Delgadino, Ph.D. dissertation, Rensselaer Polytechnic Institute, 1999 (unpublished).
[23] M. N. Kogan, *Rarefied Gas Dynamics* (Plenum, New York, 1969), p. 385.
[24] F. N. Egolfopoulos and C. K. Law, in *23rd Symposium (International) on Combustion*, 1990 (unpublished), pp. 333–340.
[25] *NIST Chemistry Webbook* 2001, http://webbook.nist.gov/chemistry/
[26] *Handbook of Chemistry and Physics*, 48th ed., edited by R. Weast (CRC Press, Boca Raton, FL, 1968).
[27] M. M. Fyrillas and A. J. Szeri, J. Fluid Mech. **277**, 381 (1994).
[28] D. Lohse, M. P. Brenner, T. F. Dupont, S. Hilgenfeldt, and B. Johnston, Phys. Rev. Lett. **78**, 1359 (1997).
[29] R. Lofstedt, K. Weninger, S. Putterman, and B. P. Barber, Phys. Rev. E **51**, 4400 (1995).